ACS OMEGA

Open Access

This article is licensed under CC-BY-NC-ND 4.0

http://pubs.acs.org/journal/acsodf

Article

Large-Area Synthesis and Fabrication of Few-Layer hBN/Monolayer RGO Heterostructures for Enhanced Contact Surface Potential

Chinnasamy Sengottaiyan, Masanori Hara, Hiroki Nagata, Hibiki Mitsuboshi, Chellamuthu Jeganathan, and Masamichi Yoshimura*

Cite This: *ACS Omega* 2024, 9, 26307−26315

Read Online

ACCESS | Metrics & More | Article Recommendations | Supporting Information

ABSTRACT: Hexagonal boron nitride (hBN) has a property similar to that of graphene, and it has become one of the most popular materials due to its flexible physical and chemical properties for a variety of applications, especially in nanoelectronics. Enhanced properties of hBN-based heterostructures are crucial for future electronic devices. In this work, a sheet-like hBN crystal was synthesized and transferred onto SiO_2/Si substrate and reduced graphene oxide (RGO)/SiO_2/Si substrate. Accordingly, the hBN and hBN/RGO films are investigated by optical microscopy, X-ray diffraction, high-resolution transmission electron microscopy, Raman spectroscopy, and atomic force microscopy. The thickness of a single hBN layer is approximately 0.4 nm. A few layers of hBN stacked in large areas are mostly observed in both hBN and the hBN/RGO films. By using Kelvin probe force microscopy, it was found that the hBN/RGO heterostructure has a contact surface potential higher than that of the hBN layer. The large-scale synthesis and fabrication of hBN/RGO films could be extended to fabricate other van der Waals heterostructures.

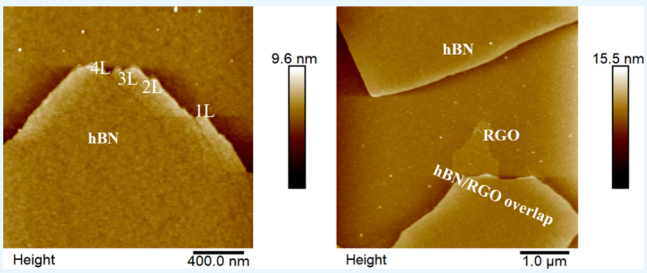

1. INTRODUCTION

Emerging 2D materials and the fabrication of their heterostructures offer exciting prospects for next-generation quantum, electrochemical, photonic, and electronic device applications.[1−3] According to previous reports, efficient heat dissipation in high-speed integrated electronic devices is a key factor in further improving their performance and consistency.[4,5] Besides, graphene and boron nitride are flexible 2D materials that offer a wide range of applications owing to their unique surface properties and atmospheric stability.[6−8]

Hexagonal boron nitride (hBN) is more attractive because of its low dielectric constant and high thermal stability compared to other phases such as cubic BN (c-BN), wurtzite BN (w-BN), and amorphous BN (a-BN) crystal lattices.[8−10] Thus, hBN combined with graphene heterostructures has low contact resistance at the interface and allows many holes and electrons to pass through during device operation.[11,12]

Some interesting heterostructures have been reported: hBN layers were grown on highly ordered pyrolytic graphite (HOPG) by high-temperature plasma-assisted molecular beam epitaxy (PA-MBE),[13] BN-graphene-BN heterostructures were prepared by the van der Waals (vdW) approach with polymer-free assembly,[14,15] chemical vapor deposition (CVD)-grown 2D materials (hBN and graphene) were transferred by electrochemical delamination,[16,17] graphene or hBN was developed on an expensive catalyst substrate of platinum,[18,19] and the single-crystalline bulk hBN or graphite was mechanically transferred by manipulation processes.[20−22] These heterostructures were extensively analyzed for their surface and electrical properties. Factors such as surface contamination, interfacial bonding, material compatibility, and processing conditions could play important roles in determining the cleanliness and quality of contacts. Therefore, the assembly of heterostructure films using a simple technique is crucial for practical applications.

The CVD method is based on the dissolution and separation of boron and nitrogen atoms using transition metal catalysts, which appears to be a more favorable route for the synthesis of high-quality hBN.[17,23−26] Significant safety and economic factors should be considered if the method involves toxic precursors and expensive machinery.[24] One of the key challenges for the large-scale fabrication of hetero 2D thin films is the transfer process of one 2D film and the integration of other 2D.[27−30] However, this is not scalable for practical applications, where films require a uniform distribution of a large number of hBN/graphene structures over a large area.

In this work, a low-cost approach to synthesize hBN with a few nanometers thickness is developed to overcome the above limitations. For the first time, we developed hBN on an RGO

Received: March 6, 2024
Revised: April 28, 2024
Accepted: May 8, 2024
Published: June 3, 2024

© 2024 The Authors. Published by American Chemical Society

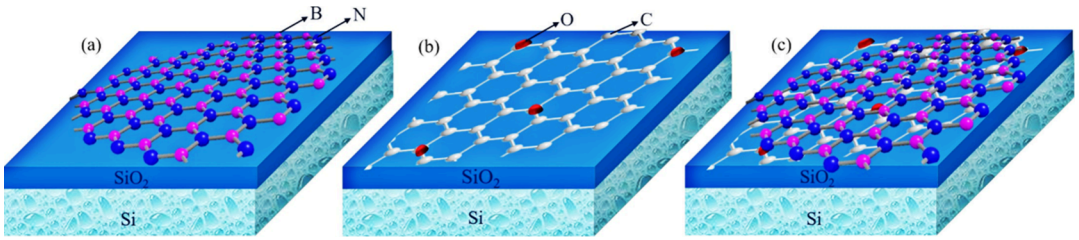

Figure 1. Fabrication of (a) hBN, (b) RGO, and (c) hBN/RGO on SiO_2/Si substrates.

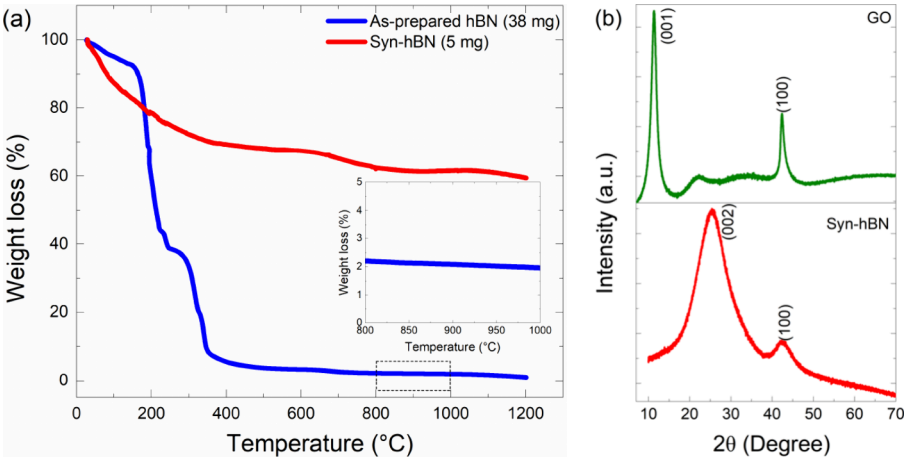

Figure 2. (a) TGA curves of the as-prepared material and syn-hBN, with an enlarged TGA curve of the as-prepared hBN shown in the inset, and (b) XRD patterns of synthesized GO and syn-hBN.

film by using a drop-casting method with a simple solution process. The fabricated heterostructures of hBN/RGO exhibit interesting surface and electrical properties that are different from those of the hBN and RGO films. The low-cost fabrication of 2D−2D heterostructures and their improved surface properties represent a new direction for fabricating other multiheterostructures, improving device performance.

2. EXPERIMENTAL SECTION

2.1. Materials. Boric acid (H_3BO_3, Wako), urea (CH_4N_2O, Wako), graphite powder (Alfa Aesar), sulfuric acid (H_2SO_4), silicon/silicon dioxide (Si/SiO_2) substrate, potassium permanganate ($KMNO_4$), sodium nitrate ($NaNO_3$), hydrochloric acid (HCl), dimethylformaldehyde (DMF), distilled water, and ethanol are used for the synthesis processes without further purification steps.

2.2. Synthesis of hBN. hBN was prepared using the following procedures: 100 mL of deionized water was combined with boric acid and urea in a molar ratio of 1:24, and the mixture was stirred at 80 °C. After complete evaporation of the water, the resulting white solid sample was referred to as-prepared hBN. The as-prepared hBN was placed into a tube furnace and heated for 5 h at various temperatures under an N_2 environment with a flow rate of 100 cc/mL (Figure S1a). After the reaction, the oven was cooled naturally, and the resulting samples were used for further testing. It is worth noting that the synthesized hBN (syn-hBN) at 900 °C exhibits a sheet-like morphology (Figure S2). Thus, syn-hBN can be used for thin film fabrications.

2.3. Fabrication of RGO Film. The modified Hummers' method was used to synthesize graphene oxide (GO),[31,32] and the reduced graphene oxide (RGO) film was prepared according to our previous report.[33] In detail, the SiO_2/Si substrate was cleaned with acetone and distilled water, followed by UV−O_3 plasma treatment (TC-003, Meiwafosis.Co., Ltd.), which was performed to remove all chemical residues and improve the hydrophilicity. GO was dispersed in DMF (1 mg/mL), followed by ultrasonication and centrifugation, which were performed several times to remove bulk GO flakes. The exfoliated GO was then dispersed in a stoichiometric amount of DMF. Afterward, a 5 μL portion of the GO dispersion was spin-coated at 3000 rpm for 10 min. The prepared GO film was dried at 80 °C overnight. Finally, the conversion from GO to RGO film was achieved through ethanol-assisted heat treatment at 800 °C for 1 h in 3% H_2/Ar by using a homemade quartz furnace.

2.4. Fabrication of hBN and hBN/RGO Films. The prepared RGO film or SiO_2/Si substrate was used for the UV−O_3 plasma treatment. Subsequently, the synthesized hBN (1 mg) was dispersed in ethanol (5 mL), and the ultrasonication and centrifugation were repeated several times to remove bulk hBN flakes. The exfoliated hBN was dispersed in ethanol, and 10 μL of the hBN dispersion was drop-cast onto an RGO film or SiO_2/Si substrate and then dried at 60 °C for 2 h. The resulting hBN or hBN/RGO film is examined for further characterization. The stages of fabrication development for RGO, hBN, and hBN/RGO films are listed in Figure 1.

2.5. Characterization. The crystal structure was examined using a Rigaku Miniflux X-ray diffractometer (XRD) with CuKα radiation (λ = 0.70932 Å). Thermal stability and structural changes were measured by thermogravimetric analysis (TGA, DTG-60H SHIMADZU). The morphology of the samples was examined using a scanning electron microscope (SEM, HITACHI, S-4700) and a transmission electron microscope (TEM, JEOL JEM 2100-Plus) at 100 kV. Before the TEM measurement, the syn-hBN was dispersed in

https://doi.org/10.1021/acsomega.4c02219
ACS Omega 2024, 9, 26307−26315

ethanol (1 mg/mL), and 20 μL of the dispersed hBN was dropped onto a Cu-grid, followed by drying at 80 °C for 2 h. Prior to SEM imaging, the synthesized and fabricated samples were coated with gold (Quorum 300T D) to avoid overcharging of the samples. Raman spectra and mapping were recorded with a RENISHAW InVia Raman spectrometer (λ = 532 nm). The chemical composition and band structure of the syn-hBN and fabricated films were characterized by X-ray photoelectron spectroscopy (XPS, Ulvac-PHI Inc., model PHI 5000 Versaprobe II). The surface structure and the potential of the fabricated films were determined using an atomic force microscope (AFM) and a Kelvin probe microscope (KPFM) (Multimode 8, Bruker). The conductive microcantilever was used with a spring constant of 2 N m^{-1} and a resonance frequency of 70 kHz (OPUS, 240AC-PP).

3. RESULTS AND DISCUSSION

3.1. Structural Evaluation of syn-hBN and GO. *3.1.1. XRD and TGA.* The thermal stabilities of the as-prepared hBN (35 mg) and the synthesized hBN (5 mg) are examined by the thermal gravimetric analysis (TGA) measurement (Figure 2a). It is noted that the synthesized hBN has a higher thermal stability than the as-prepared hBN. The as-prepared hBN shows three stages. The first stage occurs at 30−100 °C, which corresponds to the desorption of water molecules.[34] The second stage at 100−250 °C is the decomposition of the hydroxyl groups. The third stage occurs at 250−400 °C and refers to the interruption and decomposition of amine and the formation of carbonyl groups.[35,36] The gradual weight loss at 400−1200 °C is the formation of boron nitride from amorphous to crystalline nature and subproducts such as HBO_2, $H_2B_4O_7$, and B_2O_3.[37] After completion of the TGA measurement at 1200 °C, about 1 mg of boron nitride was finally obtained (inset Figure 2a). Note that hBN exhibits constant stability in the temperature range of 800−1000 °C, indicating that the phase structure was maintained. For further evidence, Figures S1b and S2d clearly show that above 1000 °C, the hBN changes in crystallinity and morphology as well. It was also found that hBN synthesized at high temperatures can be easily functionalized using organic solvents.[38] Significantly, the syn-hBN (900 °C) material has thermal stability from 250 °C after removing some hydroxyl groups and impurities from the air-stored state. The crystallinity of GO and hBN samples synthesized at different temperatures is investigated by using XRD, as shown in Figures 2b and S1b. The syn-hBN shows characteristic peaks at 2θ = 25.5 and 42.6, corresponding to (002) and (100) planes, respectively,[39,40] and GO exhibits peaks at 2θ = 11.3 and 41.5, which are (001) and (100) planes, respectively.[32] Note that no additional peaks can be seen, which confirms the purity of the synthesized materials, and further crystallinity of hBN is investigated by HR-TEM.

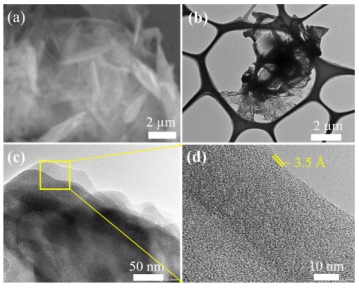

Figure 3. (a) SEM, (b,c) TEM, and (d) HR-TEM images of syn-hBN.

3.1.2. SEM and TEM. The surface morphology of syn-hBN is shown in Figure 3. The low-magnification SEM and TEM images inFigures 3a,b and S3 show an aggregated sheet-like morphology. Figures 3c and S3c show the layered or few-layered interactions of hBN. The syn-hBN exhibits an improved crystalline nature, which is evident in clear lattice fringes with an interlayer spacing of $d_{(002)}$ = ∼3.5 Å,[41,42] as seen in the HR-TEM image (Figures 3d and S3d). Based on the TGA results, the BN synthesized at different temperatures showed different morphologies, such as aggregated particles, sheets, and flakes (Figure S2). In addition, an atomic ratio of 1:0.91 of B and N was observed in syn-hBN, corresponding to the N deficiency in dominance of oxygen,[43] and a uniform distribution of B and N atoms was confirmed in the EDS mapping and their spectra (Figure S4).

3.2. Thin Film Results. *3.2.1. Optical and SEM Images.* Figure 4 shows optical microscopy and SEM images, confirming that RGO and hBN films have layered/sheet structures uniformly distributed on SiO_2/Si substrates. The RGO sheets exhibited a rough surface compared to the silicon substrate (Figures 4a and S5), and the SEM image showed a

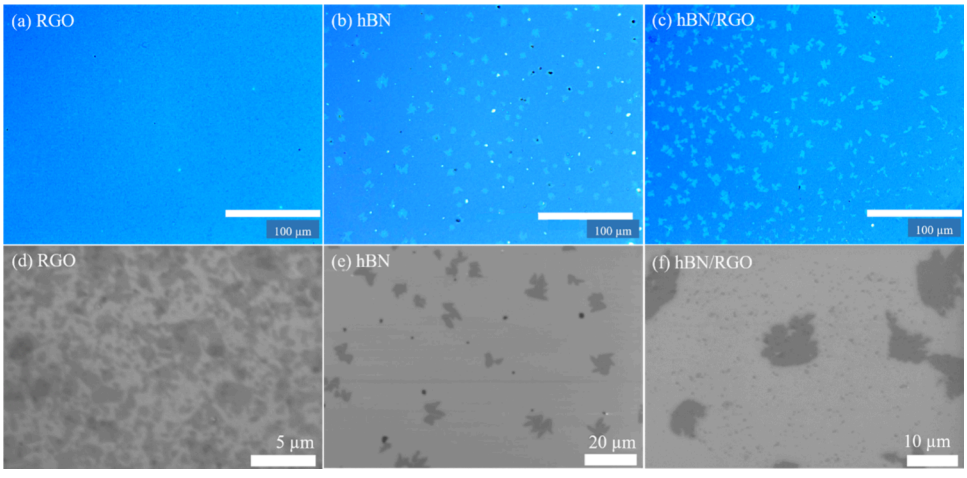

Figure 4. (a−c) Optical microscope images of RGO, hBN, and hBN/RGO films and (d−f) SEM images of the RGO, hBN, and hBN/RGO films.

https://doi.org/10.1021/acsomega.4c02219
ACS Omega 2024, 9, 26307−26315

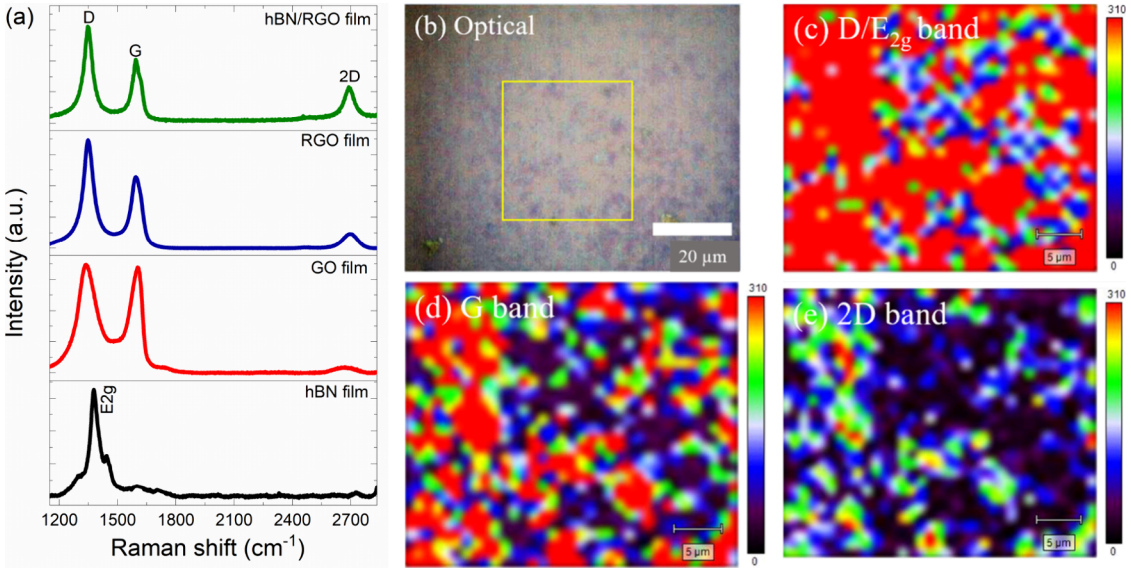

Figure 5. (a) Raman spectra of hBN, GO, RGO, and hBN/RGO films. Raman mapping of the hBN/RGO film: (b) optical image and its selected area, with corresponding maps of the D, G, and 2D bands in parts (c–e).

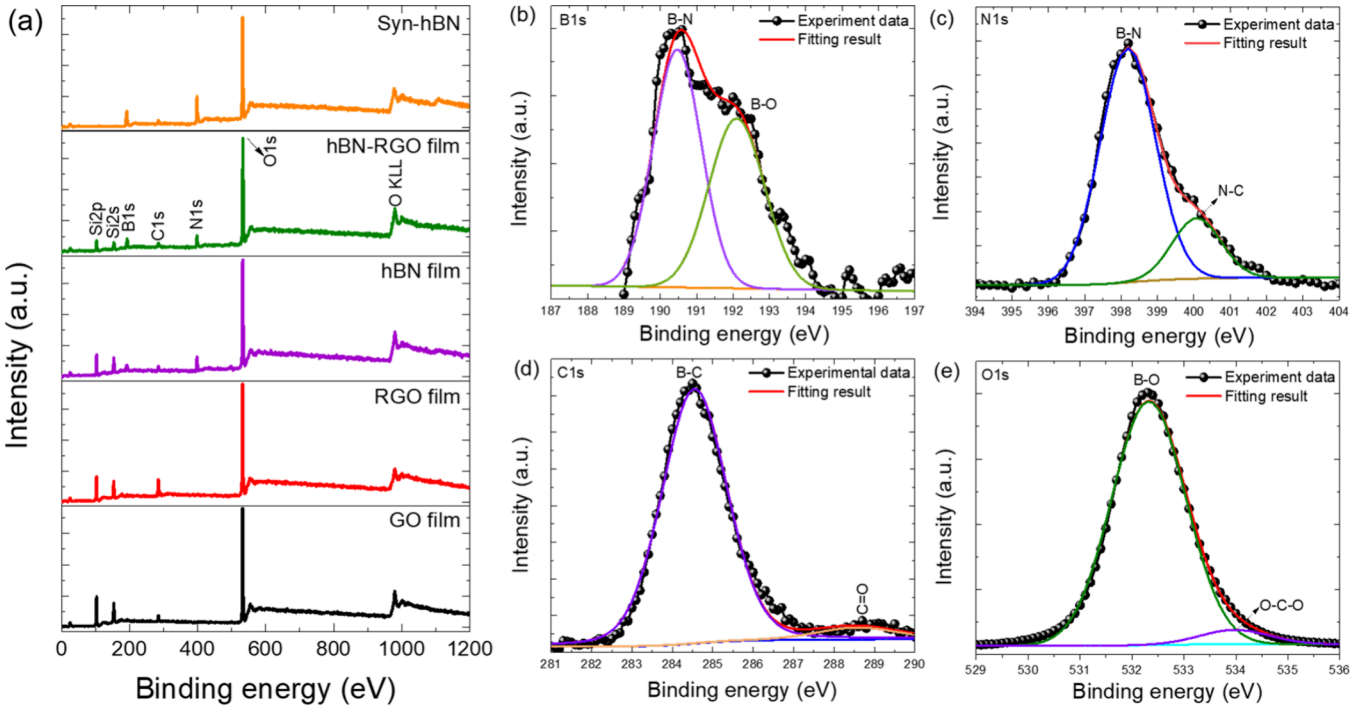

Figure 6. XPS survey spectra of (a) GO, RGO, hBN, hBN/RGO films, and syn-hBN and XPS deconvolution spectra of hBN/RGO film: (b) B 1s, (c) N 1s, (d) C 1s, and (e) O 1s.

high distinguishability of the RGO sheets (Figure 4d). In the optical images, the hBN layers were evenly distributed on the SiO_2/Si substrate (Figure 4b) and the RGO film (Figure 4c). However, the shape and size of 2D hBN were varied (Figure 4e). Previous studies have reported similar surface structures on copper foil, which were subsequently transferred to silicon substrates.[32,44] Figure 4f illustrates the layered structure in the RGO/hBN film, which is consistent with the observations in both the RGO and the hBN films.

3.2.2. Raman Spectra. The chemical structure of RGO and hBN was investigated by Raman spectroscopy, as shown in Figure 3. The hBN film exhibits a peak at 1377 cm^{-1} corresponding to the E_{2g} vibrational mode of the B–N bond.[45] The secondary shoulder peak on the E_{2g} band is attributed to impurities from the carbon or silicon.[46,47] The reduction was confirmed by the I_D/I_G ratio, with calculated values of 1.03 (GO) and 1.48 (RGO), respectively (Figure 5a).[32,48] However, the I_D/I_G ratio of the heterostructure hBN/RGO does not provide any information about the defect density or the degree of graphitization due to the overlap of the D and E_{2g} bands.[49] Notably, the D band in hBN/RGO exhibits a redshift of about 30 cm^{-1} and covers the shoulder peak compared to hBN (Figure S6a). The hBN/RGO film shows peaks at 1346, 1590, and 2691 cm^{-1}, which can be assigned to

https://doi.org/10.1021/acsomega.4c02219
ACS Omega 2024, 9, 26307−26315

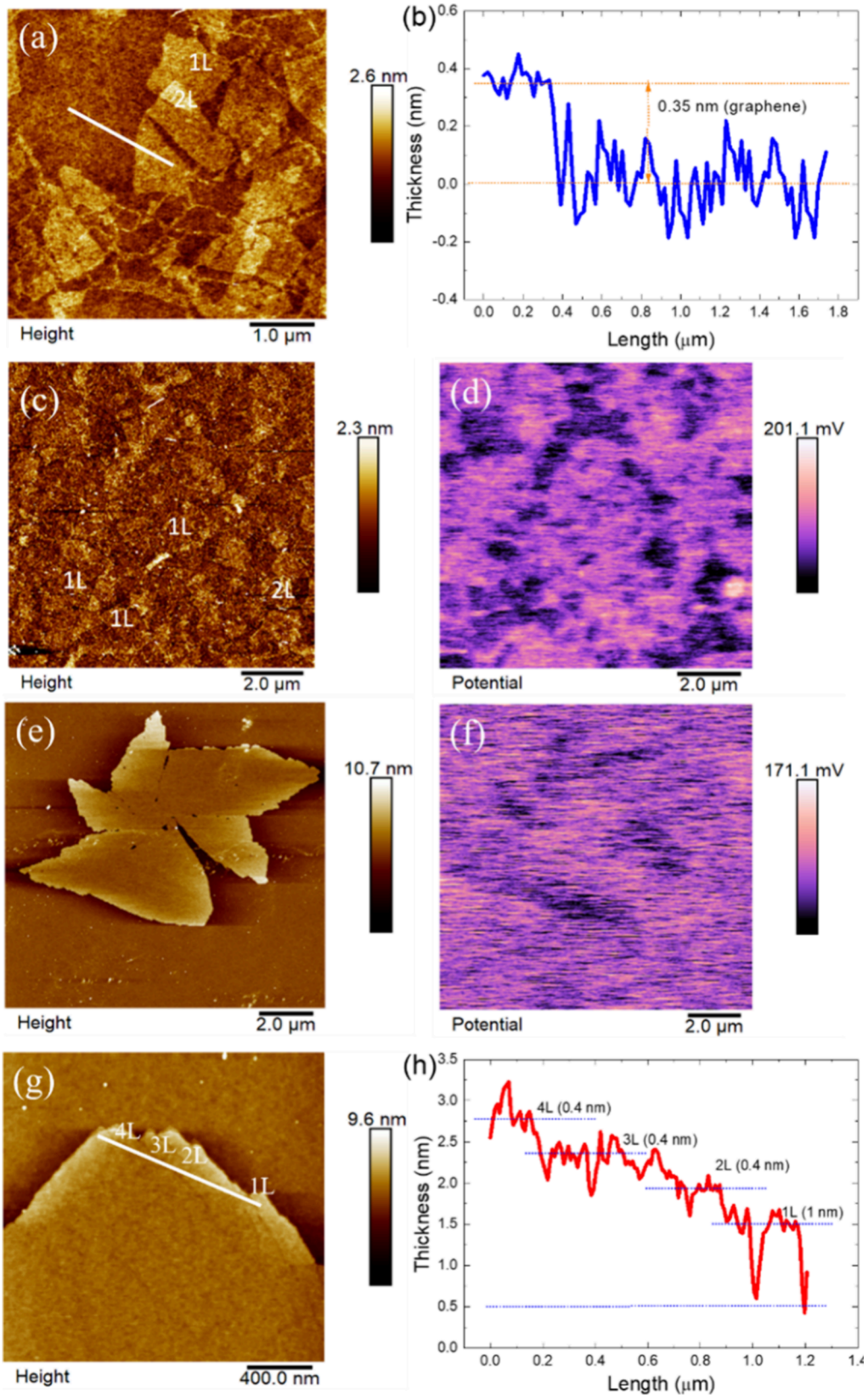

Figure 7. RGO film results: (a) AFM image, (b) height profile, and (c) AFM image with corresponding (d) KPFM. hBN film results: (e) AFM image with corresponding (f) KPFM and (g) AFM image with corresponding (h) height profile.

the D with E_{2g} (hBN), G, and 2D bands, respectively.[50] The intensity of the 2D bands of RGO and hBN/RGO films was increased compared to the GO film, attributable to the removal of oxygen and the increasing graphitization in RGO. This was evident in the Raman mapping of the hBN/RGO film, which

https://doi.org/10.1021/acsomega.4c02219
ACS Omega 2024, 9, 26307−26315

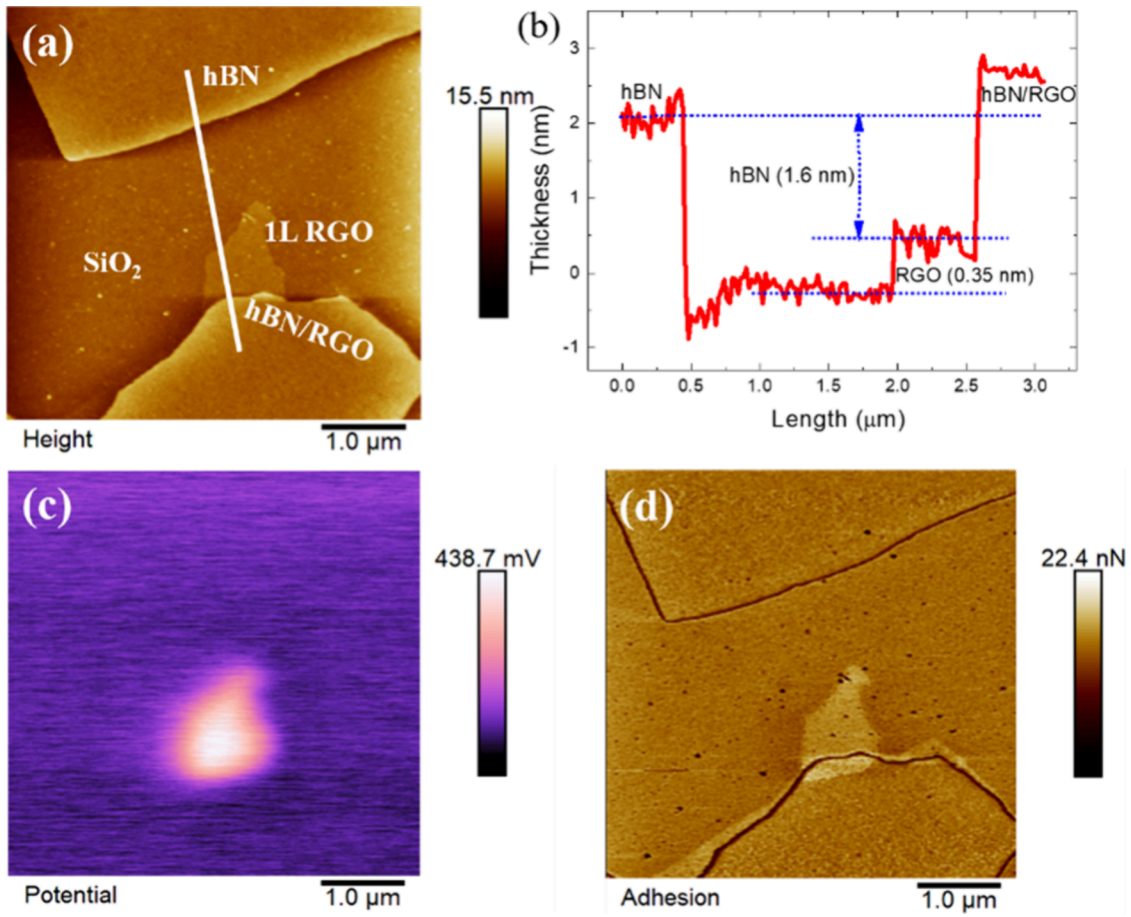

Figure 8. hBN/RGO film: (a) AFM image with the corresponding (b) height profile, (c) KPFM image, and (d) adhesion force image.

compared the intensity ratio of the individual bands (Figures 5b and S6b).

3.2.3. XPS. The chemical compositions and bonding state of the fabricated films were confirmed using XPS. The survey XPS spectra confirmed the existence of carbon, oxygen, boron, and nitrogen (Figure 6a). The deconvolution spectra show the bonding state of the composite (Figure 6b–e). The B 1s spectra from hBN/RGO and hBN films were observed with two peaks at 190.5 and 192.1 eV, corresponding to the B–N and B–O bonds, respectively (Figures 6b and S7a).[51] Furthermore, carbonaceous species are formed during the high-temperature synthesis of hBN, and oxygen-containing compounds result from the oxidation of boron in the precursor sources.[26,49] The heterostructure film exhibited a petite redshift due to the vdW interaction between two different hexagonal lattice structures consisting of C=C and B–N during the fabrication of the film. In the N 1s spectra (Figures 6c and S7b), two peaks appear at 398.1 and 399.2 eV, corresponding to N–B and N–H bonds, respectively.[52−54] The peak at 284.5 eV is attributed to sp^2 (C=C), while the peak at 288.6 eV can be assigned to C=O (Figures 6d and S8c).[33] The C–O peak on GO is higher than that on RGO, which is evident in the heat reduction under N_2/H_2 (Figure S8). In the O 1s deconvolution spectra (Figures 6e and S8d), the large peak at 532.5 eV is assigned to C–O and the weak peak at 533.6 eV could be attributed to an O–C–O.[55]

3.2.4. AFM and KPFM Images. Figure 7 shows AFM images of RGO and hBN. In Figure 7a, we observed distributions of single-layer RGO, and in some places, an overlap of two single-layer RGO sheets was observed. The average thickness of single-layer RGO was determined to be ∼0.35 nm (Figure 7b).[56,57] The uniform and large-area distribution of the RGO layers is shown in Figure 7c. This arrangement was observed across the entire substrate, indicating the fabrication of mostly continuous monolayer films over large areas with a few areas of bilayer RGO surface (Figure 7c). The absence of aggregated or wrinkled RGO layers across a large area offers potential benefits for practical applications, especially in graphene devices. This characteristic could serve as a beneficial factor for creating a conductive RGO substrate, especially when considering the expensive deposition of gold and silver in electronic applications. However, the corresponding surface potential map is evident in the KPFM image (Figure 7d). In Figures 7e and S9, the flower-like 2D hBN layer can be seen on a large scale. Figure 7f shows the local potential difference of Figure 7e. Note that the hBN layer has smaller potential (∼30 mV) differences compared to the RGO layer. The electrical resistivity of hBN is quite high,[11,58] so the hBN may shield the high-temperature operation and avoid short circuits in the devices. Thus, we conclude that the heterostructure film of hBN/RGO compensates for all of these rectifying necessities. Figures 7g and S10 show the topographic AFM images, which revealed a clear layer-by-layer stacking of the hBN. The number of layers was calculated by the thickness of each layer from the SiO_2/Si surface. The layers comprised 1 to 4 hBN layers, and the thickness of each layer was estimated to be 0.4 nm (Figure 7h), which agrees with the monolayer thickness of hBN.[58−60]

https://doi.org/10.1021/acsomega.4c02219
ACS Omega 2024, 9, 26307−26315

The vdW heterostructures of hBN/RGO are illustrated in Figure 8, and it can be observed that the RGO and hBN layers are stacked at the heterojunction, as shown in Figures 8a and S11. The height difference of the hBN was ∼1.6 nm (Figure 8b), which corresponds to a stacking of 4 hBN layers. We have already confirmed that the monolayer thickness is 0.4 nm from Figure 7g. In the stacked heterojunction region, the height of the RGO is about 0.35 nm (Figure 8b), which is similar to a monolayer RGO thickness from Figure 7b. Figure 8c shows the corresponding KPFM image of the hBN/RGO film, providing insight into the surface potential difference observed within the heterostructures. In general, some factors may affect the measurement of the potential map, such as the lift height of the probe, the probe tip, the biased voltage, and surface adsorption. Therefore, we use the following formulas 1 and 2 to estimate the contact surface potential difference (CPD) between the RGO, hBN, and probe tip.[61−63]

$$\mathrm{CPD}_{\mathrm{hBN}} = \Phi_{\mathrm{tip}} - \Phi_{\mathrm{hBN}} \quad (1)$$

$$\mathrm{CPD}_{\mathrm{RGO}} = \Phi_{\mathrm{tip}} - \Phi_{\mathrm{RGO}} \quad (2)$$

where Φ_{tip}, Φ_{RGO}, and Φ_{hBN} are the work functions of the AFM tip, RGO, and hBN, respectively. Thus, the difference in contact surface potential between RGO and hBN was estimated to be 205 mV (Figure 8c). The fact that uniform films of hBN/RGO and RGO were easily obtained, but the heterostructure film was a quiet challenge for the desired uniformity due to the hydrophobic nature of the RGO film. In the AFM image of the hBN/RGO heterostructure, a flat film structure with a few-layer thickness was observed, similar to those of RGO or hBN films. Additionally, KPFM results of the hBN/RGO heterostructure indicated enhanced contact surface potential values compared with those of the RGO or hBN films. This phenomenon could arise due to various factors such as charge transfer between the two materials, interface effects, or changes in the electronic structure upon their combination. However, a comprehensive analysis is necessary to fully elucidate the underlying mechanisms. Note that this work does not require expensive deposition or sputtering machines to fabricate the film. We believe that our approach is potentially scalable and that the fabrication of large-area hBN/RGO films may promote the efficient creation of vdW heterostructures in future nanoelectronic devices.

4. CONCLUSIONS

We have successfully synthesized scalable 2D hBN and fabricated exfoliated hBN with a controlled thickness. The calculated thicknesses of the monolayer and few-layer hBN were 0.4 and 1.9 nm, respectively. The few-layer thickness of hBN was effectively reproduced by using an RGO film. Raman mapping and XPS studies on hBN/RGO heterostructures confirmed structural deformation and graphitization growth behavior, supported by the RGO film's higher I_D/I_G values (1.48) compared to the GO film (1.03). In the AFM results of the hBN/RGO heterostructure, similar surface properties were observed for both the hBN (0.4 nm) and RGO (0.35 nm) thicknesses. Furthermore, the KPFM results of the hBN/RGO heterostructure indicated a higher contact surface potential of 205 mV compared with those of the RGO and hBN films. The proposed work offers a cost-effective approach for the mass production of hBN with the desired two-dimensional structure for both solid-state and thin film applications.

ASSOCIATED CONTENT

Supporting Information

The Supporting Information is available free of charge at https://pubs.acs.org/doi/10.1021/acsomega.4c02219.

Digital photos of hBN samples, XRD patterns of synthesized hBN at different temperatures, as well as additional data including SEM images, elemental dispersive X-ray spectra (EDX), elemental mapping, TEM/HR-TEM images, Raman spectra, and additional AFM and KPFM results for detection and comparison (PDF)

AUTHOR INFORMATION

Corresponding Author

Masamichi Yoshimura − *Toyota Technological Institute, Tempaku, Nagoya, Aichi 468-8511, Japan*; Email: yoshi@toyota-ti.ac.jp

Authors

Chinnasamy Sengottaiyan − *Toyota Technological Institute, Tempaku, Nagoya, Aichi 468-8511, Japan*; orcid.org/0000-0001-9224-3699

Masanori Hara − *Toyota Technological Institute, Tempaku, Nagoya, Aichi 468-8511, Japan*

Hiroki Nagata − *Toyota Technological Institute, Tempaku, Nagoya, Aichi 468-8511, Japan*

Hibiki Mitsuboshi − *Toyota Technological Institute, Tempaku, Nagoya, Aichi 468-8511, Japan*

Chellamuthu Jeganathan − *Toyota Technological Institute, Tempaku, Nagoya, Aichi 468-8511, Japan*

Complete contact information is available at: https://pubs.acs.org/10.1021/acsomega.4c02219

Notes

The authors declare no competing financial interest.

ACKNOWLEDGMENTS

This study received partial support from the Research Center for Smart Energy Technologies at Toyota Technological Institute (TTI), Nagoya, Japan, and from JSPS KAKENHI (22H00294). The authors would like to express their gratitude to Mrs. Tomiko Ikeda at TTI for conducting the AFM measurements.

REFERENCES

(1) Dean, C. R.; Young, A. F.; Meric, I.; Lee, C.; Wang, L.; Sorgenfrei, S.; Watanabe, K.; Taniguchi, T.; Kim, P.; Shepard, K. L.; Hone, J. Boron nitride substrates for high-quality graphene electronics. *Nat. Nanotechnol.* **2010**, *5* (10), 722−726.

(2) Geim, A. K.; Novoselov, K. S. The rise of graphene. *Nat. Mater.* **2007**, *6* (3), 183−191.

(3) Chit, S. L.; Sarthak, D.; Ivan, A. V.; Ding, H.; Yiyu, Z.; Teymour, T.-D.; Wei, F.; Dasari, V.; Kuan, E. J. G. Dielectrics for two-dimensional transition-metal dichalcogenide applications. *ACS Nano* **2023**, *17* (11), 9870−9905.

(4) Yasunori, T.; Tomohito, S.; Yi-Fei, W.; Tomoko, O.; Hiroyuki, M.; Daisuke, K.; Shizuo, T. High-speed complementary integrated circuit with a stacked structure using fine electrodes formed by reverse offset printing. *ACS Appl. Electron. Mater.* **2020**, *2* (3), 763−768.

(5) Satterthwaite, P. F.; Zhu, W.; Jastrzebska-Perfect, P.; Tang, M.; Spector, S. O.; Gao, H.; Kitadai, H.; Lu, A.-Y.; Tan, Q.; Tang, S.-Y.; Chueh, Y.-L.; Kuo, C.-N.; Lue, C. S.; Kong, J.; Ling, X.; Niroui, F. Van

der Waals device integration beyond the limits of van der Waals forces using adhesive matrix transfer. *Nat. Electron.* **2023**, *7*, 17−28.
(6) Akinwande, D.; Petrone, N.; Hone, J. Two-dimensional flexible nanoelectronics. *Nat. Commun.* **2014**, *5* (1), 5678.
(7) Vincent, T.; Panchal, V.; Booth, T.; Power, S. R.; Jauho, A.-P.; Antonov, V. N.; Kazakova, O. Probing the nanoscale origin of strain and doping in graphene-hBN heterostructures. *2D Mater.* **2019**, *6* (1), No. 015022.
(8) Sutter, P.; Cortes, R.; Lahiri, J.; Sutter, E. Interface formation in monolayer graphene-boron nitride heterostructures. *Nano Lett.* **2012**, *12* (9), 4869−4874.
(9) Li, J.; Yuan, C.; Elias, C.; Wang, J.; Zhang, X.; Ye, G.; Huang, C.; Kuball, M.; Eda, G.; Redwing, J. M.; He, R.; Cassabois, G.; Gil, B.; Valvin, P.; Pelini, T.; Liu, B.; Edgar, J. H. Hexagonal boron nitride single crystal growth from solution with a temperature gradient. *Chem. Mater.* **2020**, *32* (12), 5066−5072.
(10) Naclerio, A. E.; Kidambi, P. R. A review of scalable hexagonal boron nitride (h-BN) synthesis for present and future applications. *Adv. Mater.* **2023**, *35* (6), No. 2207374, DOI: 10.1002/adma.202207374.
(11) Chernozatonskii, L. A.; Demin, V. A.; Bellucci, S. Bilayered graphene/h-BN with folded holes as new nanoelectronic materials: modeling of structures and electronic properties. *Sci. Rep.* **2016**, *6* (1), 38029.
(12) Liu, Z.; Luiz; Sato, Y.; Lin, Y.; Yeh, C.; Chiu, P.; Terauchi, M.; Iijima, S.; Suenaga, K. Postsynthesis of h-BN/graphene heterostructures inside a STEM. *Small* **2016**, *12* (2), 252−259.
(13) Román, R. J. P.; Costa, F. J. R. C.; Zobelli, A.; Elias, C.; Valvin, P.; Cassabois, G.; Gil, B.; Summerfield, A.; Cheng, T. S.; Mellor, C. J.; Beton, P. H.; Novikov, S. V.; Zagonel, L. F. Band gap measurements of monolayer h-BN and insights into carbon-related point defects. *2D Mater.* **2021**, *8* (4), No. 044001.
(14) Wang, L.; Meric, I.; Huang, P. Y.; Gao, Q.; Gao, Y.; Tran, H.; Taniguchi, T.; Watanabe, K.; Campos, L. M.; Muller, D. A.; Guo, J.; Kim, P.; Hone, J.; Shepard, K. L.; Dean, C. R. One-dimensional electrical contact to a two-dimensional material. *Science* **2013**, *342* (6158), 614−617.
(15) Fukamachi, S.; Solís-Fernández, P.; Kawahara, K.; Tanaka, D.; Otake, T.; Lin, Y.; Suenaga, K.; Ago, H. Large-area synthesis and transfer of multilayer hexagonal boron nitride for enhanced graphene device arrays. *Nat. Electron.* **2023**, *6* (2), 126−136.
(16) Wang, Y.; Zheng, Y.; Xu, X.; Dubuisson, E.; Bao, Q.; Lu, J.; Loh, K. P. Electrochemical delamination of CVD-grown graphene film: Toward the recyclable use of copper catalyst. *ACS Nano* **2011**, *5* (12), 9927−9933.
(17) Cartamil-Bueno, S. J.; Cavalieri, M.; Wang, R.; Houri, S.; Hofmann, S.; van der Zant, H. S. J. Mechanical characterization and cleaning of CVD single-layer h-BN resonators. *npj 2D Mater. Appl.* **2017**, *1* (1), 1−7.
(18) Joon, H. C.; Seo, Y.; Dolocan, A.; Hall, N. A.; Cullinan, M. Monolayer graphene grown on nanoscale Pt films deposited on TiO_2 substrates for micro- and nanoelectromechanical systems. *ACS Appl. Nano Mater.* **2020**, *3* (10), 9731−9739.
(19) Park, J.-H.; Park, J. C.; Yun, S. J.; Kim, H.; Luong, D. H.; Kim, S. M.; Choi, S. H.; Yang, W.; Kong, J.; Kim, K. K.; Lee, Y. H. Large-area monolayer hexagonal boron nitride on Pt foil. *ACS Nano* **2014**, *8* (8), 8520−8528.
(20) Novoselov, K. S.; Geim, A. K.; Morozov, S. V.; Jiang, D.; Zhang, Y.; Dubonos, S. V.; Grigorieva, I. V.; Firsov, A. A. Electric field effect in atomically thin carbon films. *Science* **2004**, *306* (5696), 666−669.
(21) Zeng, F.; Wang, R.; Wei, W.; Feng, Z.; Guo, Q.; Ren, Y.; Cui, G.; Zou, D.; Zhang, Z.; Liu, S.; Liu, K.; Fu, Y.; Kou, J.; Wang, L.; Zhou, X.; Tang, Z.; Ding, F.; Yu, D.; Liu, K.; Xu, X. Stamped production of single-crystal hexagonal boron nitride monolayers on various insulating substrates. *Nat. Commun.* **2023**, *14* (1), 6421.
(22) Hattori, Y.; Taniguchi, T.; Watanabe, K.; Kitamura, M. Identification of the monolayer thickness difference in a mechanically exfoliated thick flake of hexagonal boron nitride and graphite for van der Waals heterostructures. *Nanotechnology* **2023**, *34* (29), 295701−295701.
(23) Cai, Q.; Scullion, D.; Gan, W.; Falin, A.; Zhang, S.; Watanabe, K.; Taniguchi, T.; Chen, Y.; Santos, E. J. G.; Li, L. H. High thermal conductivity of high-quality monolayer boron nitride and its thermal expansion. *Sci. Adv.* **2019**, *5* (6), No. eaav0129.
(24) Watanabe, K.; Taniguchi, T. Far-UV photoluminescence microscope for impurity domain in hexagonal-boron-nitride single crystals by high-pressure, high-temperature synthesis. *npj 2D Mater. Appl.* **2019**, *3* (1), 40 DOI: 10.1038/s41699-019-0124-4.
(25) Sharma, S.; Kalita, G.; Vishwakarma, R.; Zulkifli, Z.; Tanemura, M. Opening of triangular hole in triangular-shaped chemical vapor deposited hexagonal boron nitride crystal. *Sci. Rep.* **2015**, *5* (1), No. 10426, DOI: 10.1038/srep10426.
(26) Singh, R.; Kalita, G.; Mahyavanshi, R. D.; Adhikari, S.; Uchida, H.; Tanemura, M.; Umeno, M.; Kawahara, T. Low temperature wafer-scale synthesis of hexagonal boron nitride by microwave assisted surface wave plasma chemical vapour deposition. *AIP Advances* **2019**, *9* (3), No. 035043, DOI: 10.1063/1.5091529.
(27) Pham, P. V.; Bodepudi, S. C.; Shehzad, K.; Liu, Y.; Xu, Y.; Yu, B.; Duan, X. 2D heterostructures for ubiquitous electronics and optoelectronics: Principles, opportunities, and challenges. *Chem. Rev.* **2022**, *122* (6), 6514−6613.
(28) Novoselov, K. S.; Mishchenko, A.; Carvalho, A.; Castro Neto, A. H. 2D materials and van der Waals heterostructures. *Science* **2016**, *353* (6298), No. aac9439.
(29) Schranghamer, T. F.; Sharma, M.; Singh, R.; Das, S. Review and comparison of layer transfer methods for two-dimensional materials for emerging applications. *Chem. Soc. Rev.* **2021**, *50* (19), 11032−11054.
(30) Wang, S.; Wang, X.; Warner, J. H. All chemical vapor deposition growth of MoS_2:h-BN vertical van der Waals heterostructures. *ACS Nano* **2015**, *9* (5), 5246−5254.
(31) Sengottaiyan, C.; Jayavel, R.; Bairi, P.; Shrestha, R. G.; Ariga, K.; Shrestha, L. K. Cobalt oxide/reduced graphene oxide composite with enhanced electrochemical supercapacitance performance. *Bull. Chem. Soc. Jpn.* **2017**, *90* (8), 955−962.
(32) Sengottaiyan, C.; Kalam, N. A.; Jayavel, R.; Shrestha, R. G.; Subramani, T.; Sankar, S.; Hill, J. P.; Shrestha, L. K.; Ariga, K. $BiVO_4$/RGO hybrid nanostructure for high performance electrochemical supercapacitor. *J. Solid State Chem.* **2019**, *269*, 409−418.
(33) De Silva, K. K. H.; Shibata, K.; Viswanath, P.; Huang, H.; Yoshimura, M. High-quality monolayer reduced graphene oxide films via combined chemical reduction and ethanol-assisted defect restoration. *Adv. Mater. Interfaces* **2022**, *9*, No. 2200503.
(34) Rvai Kumar, G.; Raja Pugalenthi, M.; Cao, G.; Manimuthu, R. P. Reinforced hydroxylated boron nitride on porous sulfonated poly(ether sulfone) with excellent electrolyte properties for H_2/O_2 fuel cells. *Energy Fuels* **2022**, *36* (12), 6445−6458.
(35) Nurunnabi, M.; Nafiujjaman, M.; Lee, S.-J.; Park, I.-K.; Huh, K. M.; Lee, Y. Preparation of ultra-thin hexagonal boron nitride nanoplates for cancer cell imaging and neurotransmitter sensing. *Chem. Commun.* **2016**, *52* (36), 6146−6149.
(36) Hernández, M. F.; Suárez, G.; Cipollone, M.; Conconi, M. S.; Aglietti, E. F.; Rendtorff, N. M. Formation, microstructure and properties of aluminum borate ceramics obtained from alumina and boric acid. *Ceram. Int.* **2017**, *43* (2), 2188−2195.
(37) Jähnichen, T.; Hojak, J.; Bläker, C.; Pasel, C.; Mauer, V.; Zittel, V.; Denecke, R.; Bathen, D.; Enke, D. Synthesis of turbostratic boron nitride: effect of urea decomposition. *ACS Omega* **2022**, *7* (37), 33375−33384.
(38) Smith, A. D.; Martínez-Jiménez, C.; Ya'akobi, A. M.; Simonsen, C. J.; Talmon, Y.; Pasquali, M.; Martí, Á. A. Understanding the exfoliation and dispersion of hexagonal boron nitride nanosheets by surfactants: Implications for antibacterial and thermally resistant coatings. *ACS Appl. Nano Mater.* **2021**, *4* (1), 142−151.
(39) Chen, C.; Wang, J.; Liu, D.; Yang, C.; Liu, Y.; Ruoff, R. S.; Lei, W. Functionalized boron nitride membranes with ultrafast solvent

transport performance for molecular separation. *Nat. Commun.* **2018**, *9* (1), 1902 DOI: 10.1038/s41467-018-04294-6.
(40) Guerra, V.; Wan, C.; Degirmenci, V.; Sloan, J.; Presvytis, D.; McNally, T. 2D boron nitride nanosheets (BNNs) prepared by high-pressure homogenisation: Structure and morphology. *Nanoscale* **2018**, *10* (41), 19469−19477.
(41) Shi, Y.; Hamsen, C.; Jia, X.; Kim, K. K.; Reina, A.; Hofmann, M.; Hsu, A. L.; Zhang, K.; Li, H.; Juang, Z.-Y.; Dresselhaus Mildred, S.; Li, L.-J.; Kong, J. Synthesis of few-layer hexagonal boron nitride thin film by chemical vapor deposition. *Nano Lett.* **2010**, *10* (10), 4134−4139.
(42) Mittal, N.; Kedawat, G.; Kanika; Gupta, S.; Kumar Gupta, B. An innovative method for large-scale synthesis of hexagonal boron nitride nanosheets by liquid phase exfoliation. *ChemistrySelect* **2020**, *5* (40), 12564−12569.
(43) Liu, M.; Chen, C.; Du, M.; Wu, Y.; Ren, C.; Ding, K.; Song, M.; Huang, C. Porous hexagonal boron nitride sheets: effect of hydroxyl and secondary amino groups on photocatalytic hydrogen evolution. *ACS Appl. Nano Mater.* **2018**, *1* (9), 4566−4575.
(44) Kidambi, P. R.; Blume, R.; Kling, J.; Wagner, J. B.; Baehtz, C.; Weatherup, R. S.; Schlögl, R.; Bayer, B. C.; Hofmann, S. In situ observations during chemical vapor deposition of hexagonal boron nitride on polycrystalline copper. *Chem. Mater.* **2014**, *26* (22), 6380−6392.
(45) Zuo, Z.; Xu, Z.; Zheng, R.; Khanaki, A.; Zheng, J.-G.; Liu, J. In-situ epitaxial growth of graphene/h-BN van der Waals heterostructures by molecular beam epitaxy. *Sci. Rep.* **2015**, *5* (1), No. 14760, DOI: 10.1038/srep14760.
(46) Liu, D.; Chen, X.; Yan, Y.; Zhang, Z.; Jin, Z.; Yi, K.; Zhang, C.; Zheng, Y.; Yao, W.; Yang, J.; Xu, X.; Chen, J.; Lu, Y.; Wei, D.; Thye, A.; Wei, D. Conformal hexagonal-boron nitride dielectric interface for tungsten diselenide devices with improved mobility and thermal dissipation. *Nat. Commun.* **2019**, *10* (1), 1188 DOI: 10.1038/s41467-019-09016-0.
(47) Karim, M. Z.; Lopes, J.; Ramsteiner, M. The impact of ultraviolet laser excitation during Raman spectroscopy of hexagonal boron nitride thin films. *J. Raman Spectrosc.* **2020**, *51* (12), 2468−2477.
(48) Majumder, S. B.; Satpati, B.; Kumar, S.; Banerjee, S. Multifunctional reduced graphene oxide wrapped circular au nanoplatelets: Enhanced photoluminescence, excellent surface-enhanced raman scattering, photocatalytic water splitting, and non-enzymatic biosensor. *ACS Appl. Nano Mater.* **2018**, *1* (8), 3945−3955.
(49) Rastogi, P. K.; Sahoo, K. R.; Thakur, P.; Sharma, R.; Bawari, S.; Podila, R.; Narayanan, T. N. Graphene-hBN non-van der Waals vertical heterostructures for four-electron oxygen reduction reaction. *Phys. Chem. Chem. Phys.* **2019**, *21* (7), 3942−3953.
(50) Song, Y.; Zhang, C.; Li, B.; Ding, G.; Jiang, D.; Wang, H.; Xie, X. Van der Waals epitaxy and characterization of hexagonal boron nitride nanosheets on graphene. *Nanoscale Res. Lett.* **2014**, *9* (1), 367 DOI: 10.1186/1556-276X-9-367.
(51) Bresnehan, M. S.; Hollander, M. J.; Wetherington, M.; Wang, K.; Miyagi, T.; Pastir, G.; Snyder, D. W.; Gengler, J. J.; Voevodin, A. A.; Mitchel, W. C.; Robinson, J. A. Prospects of direct growth boron nitride films as substrates for graphene electronics. *J. Mater. Res.* **2014**, *29* (3), 459−471.
(52) Lin, J.; Tay, R. Y.; Li, H.; Jing, L.; Tsang, S. H.; Wang, H.; Zhu, M.; McCulloch, D. G.; Teo, E. H. T. Smoothening of wrinkles in CVD-grown hexagonal boron nitride films. *Nanoscale* **2018**, *10* (34), 16243−16251.
(53) Fernandes, J.; Queirós, T.; Rodrigues, J.; Nemala, S. S.; LaGrow, A. P.; Placidi, E.; Alpuim, P.; Nieder, J. B.; Capasso, A. Room-temperature emitters in wafer-scale few-layer hBN by atmospheric pressure CVD. *FlatChem.* **2022**, *33*, No. 100366.
(54) Wang, G.; Meng, J.; Chen, J.; Cheng, Y.; Huang, J.; Zhang, S.; Yin, Z.; Jiang, J.; Wu, J.; Zhang, X. Epitaxy of hexagonal boron nitride thin films on sapphire for optoelectronics. *Cryst. Growth Des.* **2022**, *22* (12), 7207−7214.
(55) Yu, L.; Yap, P. L.; Santos, A.; Tran, D.; Hassan, K.; Ma, J.; Lošić, D. Graphene and hexagonal boron nitride in molybdenum disulfide/epoxy composites for significant X-ray shielding enhancement. *ACS Appl. Nano Mater.* **2022**, *5* (9), 12196−12208.
(56) Kwon, S.-Y.; Lee, J. Y.; Lee, H.; Koh, S. J.; Ko, J.; Kim, Y. H.; Kim, S. O.; Park, J. Y. The effect of thickness and chemical reduction of graphene oxide on nanoscale friction. *J. Phys. Chem. B* **2018**, *122* (2), 543−547.
(57) De Silva, K. K. H.; Huang, H.-H.; Joshi, R.; Yoshimura, M. Restoration of the graphitic structure by defect repair during the thermal reduction of graphene oxide. *Carbon* **2020**, *166*, 74−90.
(58) Li, L. H.; Santos, E. J. G.; Xing, T.; Cappelluti, E.; Roldán, R.; Chen, Y.; Watanabe, K.; Taniguchi, T. Dielectric screening in atomically thin boron nitride nanosheets. *Nano Lett.* **2015**, *15* (1), 218−223.
(59) Cho, Y.-J.; Summerfield, A.; Davies, A.; Cheng, T. S.; Smith, E. F.; Mellor, C. J.; Khlobystov, A. N.; Foxon, C. T.; Eaves, L.; Beton, P. H.; Novikov, S. V. Hexagonal boron nitride tunnel barriers grown on graphite by high temperature molecular beam epitaxy. *Sci. Rep.* **2016**, *6* (1), 34474.
(60) Yi, H.; Solís-Fernández, P.; Hibino, H.; Ago, H. Surface etching and edge control of hexagonal boron nitride assisted by triangular Sn nanoplates. *Nanoscale Adv.* **2022**, *4* (18), 3786−3792.
(61) Markeev, P. A.; Najafidehaghani, E.; Gan, Z.; Sotthewes, K.; George, A.; Turchanin, A.; de Jong, M. P. Energy-level alignment at interfaces between transition-metal dichalcogenide monolayers and metal electrodes studied with Kelvin probe force microscopy. *J. Phys. Chem. C* **2021**, *125* (24), 13551−13559.
(62) Khalil, L.; Ernandes, C.; Avila, J.; Rousseau, A.; Dudin, P.; Zhigadlo, N. D.; Cassabois, G.; Gil, B.; Oehler, F.; Chaste, J.; Ouerghi, A. High p doped and robust band structure in Mg-doped hexagonal boron nitride. *Nanoscale Adv.* **2023**, *5* (12), 3225−3232.
(63) Behn, W.; Krebs, Z. J.; Smith, K. J.; Watanabe, K.; Taniguchi, T.; Brar, V. W. Measuring and tuning the potential landscape of electrostatically defined quantum dots in graphene. *Nano Lett.* **2021**, *21* (12), 5013−5020.

https://doi.org/10.1021/acsomega.4c02219
ACS Omega 2024, 9, 26307−26315